ISSN (Print) 1226-1750
ISSN (Online) 2233-6656
Journal of Magnetics 28(3), 258-267 (2023) https://doi.org/10.4283/JMAG.2023.28.3.258

Design and Analysis of the Interior Permanent-Magnet Machine Considering Slot-pole Combination and Rotor Topology

Haoen Xu, Jin Huang, Xinyu Xu, and Junqiang Zheng*

School of Electrical Engineering, Nantong University, Nantong 226019, China

(Received 20 June 2023, Received in final form 5 July 2023, Accepted 5 July 2023)

This paper presents how to select the proper slot and pole combination (SPC) and reasonable rotor topologies for an interior permanent-magnet (IPM) machine. Firstly, the selection principle of SPC is reported, and some electromagnet performances, including winding factor, stator space magneto-motive force (MMF) harmonics, radial force harmonics, and cogging torque, are analyzed and compared. Secondly, four PM rotor topologies are designed and discussed, including surface permanent-magnet (SPM), spoke type, V-shape, and multi-layer reluctance (MR) type. Their performances, such as back-EMFs, torque, and ripple and flux-weakening capability, are thoroughly analyzed and compared by the finite-element method (FEM). Finally, a 27-slot and 8-pole V-shape IPM machine is selected and designed optimally, which offers high power/torque density, high efficiency, and less torque ripple. In order to ensure the reliability of its rotor mechanical strength, the equivalent stress and deformation are analyzed by ANASY. Besides, its d-q axis mathematical model is built to verify its performance further. Then experiments on the prototypes are carried out for validation.

Keywords : Interior permanent-magnet machine, harmonic, finite-element method, rotor stress, mathematical model

1. Introduction

Permanent-magnet (PM) machines present the advantages of high power, high efficiency, and high reliability, which have broad application prospects in aerospace, ship propulsion, wind power generation, electric vehicles, and other fields [1].

Surface-mounted permanent magnet (SPM) machines are widely used among these PM machines due to their simple topology and control methods. However, its magnetic concentration effect could be better, the magnetic flux leakage between poles is considerable, and the magnets utilization rate could be higher [2]. In addition, due to the similar d-q axis inductance of the SPM machine, it is weakening magnetic field performance could be better, so it is unsuitable for some applications with broad speed regulation [3]. Moreover, this is precisely the critical performance index pursued by modern PM machines. The back-EMF of SPM machines is usually relatively large, which is also unfavorable for applications that strictly limit the DC bus voltage [4].

*Corresponding author: Tel: +86-15190823468
e-mail: zjq@ntu.edu.cn

Fig. 1 shows the structure of a traditional IPM machine, in which the d-axis and q-axis are marked. Due to the different magnetic circuit structures, the d-q axis inductance of the IPM machine is different, which is the most significant feature that distinguishes it from the SPM machine. Moreover, the IPM machine has superior magnetic concentration performance and excellent field weakening speed expansion ability, suitable for wide speed regulation applications such as electric vehicles. This feature enables the IPM machine to obtain greater

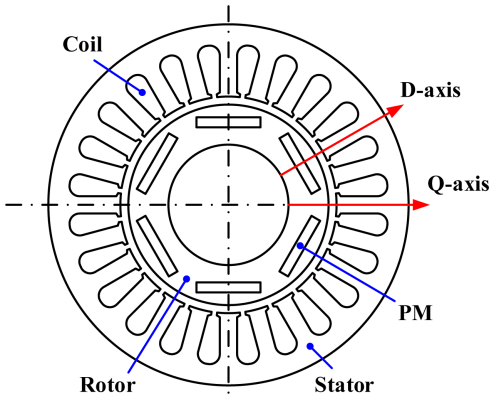

Fig. 1. (Color online) Interior permanent-magnet synchronous machine.

reluctance torque and better field-weakening speed regulation performance [5]. Furthermore, since the PM is embedded in the iron core, the PM eddy-current losses and risk of PM demagnetization are significantly reduced [6]. These two characteristics help further to improve the efficiency and reliability of the motor system [7].

Compared with the traditional integer-slot winding PM machine, the fractional-slot winding PM machine has the advantages of sinusoidal back EMF waveform, low torque ripple, and good fault tolerance performance [8]. However, the sizeable magnet-motive force (MMF) harmonics of the fractional-slot winding will cause adverse effects on the machine, such as significant eddy-current losses and electromagnetic vibration noise, and the winding factor reduction caused by the distribution effect [9-11]. Therefore, the selection of slot and pole coordination (SPC) for fractional-slot windings dramatically influences the quality of the PM machine. In addition, the structure of the IPM machine is complex and diverse. How to take into account the influence of the winding structure and rotor topology on the electromagnetic performance in the design process is of great significance to the design of a high-quality IPM machine [12].

This paper presents how to select the proper SPC and reasonable rotor topologies for an IPM machine. Section II will describe the selection principle of SPC, and some electromagnetic performances are analyzed and compared, including winding factor, space MMF harmonics, radial force harmonics, and cogging torque. In Section III, four PM rotor topologies for IPM machines will be designed. These machines include SPM, spoke type, V-shape, and multi-layer reluctance (MR) type are designed and whose performances, such as back-EMFs, torque, and its ripple and flux-weakening, will be thoroughly analyzed and compared by finite-element method (FEM). In Section IV, a 27-slot and 8-pole (27s8p) V-shape IPM machine will be selected and optimally designed to offer excellent electromagnetic performances, such as sinusoidal back-EMF, high power/torque density, less torque ripple, and high efficiency. Besides, to ensure the reliability of its rotor mechanical strength, the equivalent stress and deformation will be analyzed in Section V. Then, the d-q axis mathematical model will be built to verify its performances in Section VI. Finally, the experiments on the prototypes will be carried out for validation in Section VII.

2. Selection of Slot and Pole Combination of Fractional-slot Windings

The SPC of an IPM machine significantly affects its electromagnetic performances, such as winding factor, Stator MMF harmonics, radial force harmonics, and cogging torque. This section systematically analyzes the relationship between the SPC and these performances.

2.1. Winding factor

The winding factor is a critical performance parameter of the electrical machine, which determines the amplitude of no-load back-EMF when the condition of the PM magnetic field and rotation speed is constant. The winding factors of different SPC are presented in Table 1. Due to space constraints, the number of slots and poles are listed as 27 and 10, respectively. The numbers in parentheses on the winding factor in the table represent the winding pitch. It can be seen from Table 1 that the winding factor of the integer slot winding motor is larger than the fractional-slot winding as a whole. Compared to the 12s2p and 12s4p integer slot winding motors, the

Table 1. Winding factor of the different SPC.

	9	12	18	24	27
2	$0.945^{(4)}$	$0.966^{(6)}$	$0.960^{(9)}$	$0.958^{(12)}$	$0.954^{(13)}$
4	$0.945^{(2)}$	$1^{(3)}$	$0.945^{(4)}$	$0.966^{(6)}$	$0.941^{(6)}$
6	$0.866^{(1)}$	~	$1^{(3)}$	~	$0.945^{(4)}$
8	**$0.945^{(1)}$**	$0.866^{(1)}$	**$0.945^{(2)}$**	$1^{(3)}$	**$0.941^{(3)}$**
10	$0.945^{(1)}$	$0.933^{(1)}$	$0.945^{(2)}$	$0.925^{(2)}$	$0.941^{(3)}$

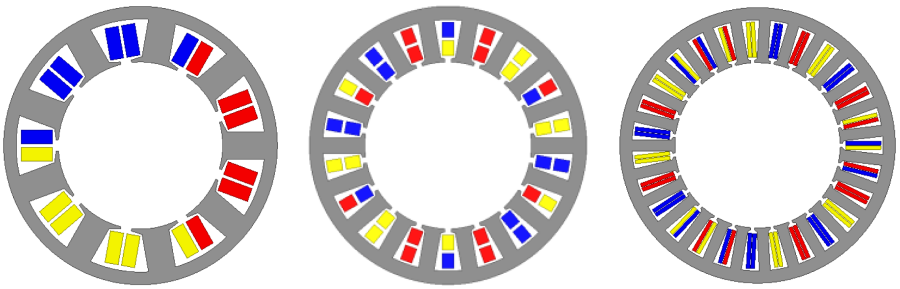

Fig. 2. (Color online) Stator strucure of different SPC PM machines. (a) 9s8p. (b) 18s8p. (c) 27s8p.

smaller the number of slots per pole and each phase, the more significant the winding factor. For fractional slot winding motors, when the pitch is the same, the closer the number of slot poles is, the more significant the winding factor will be. The different SPC PM machines of the 9s8p, 18s8p, and 27s8p winding factors, 0.945, 0.945, and 0.941, are selected for further study. Their finite-element model is shown in Fig. 2. It can be seen that their span of the winding is 1, 2, and 3, respectively. Red, yellow, and blue coils represent the A, B, and C phases. For a fair comparison, they are designed based on identical size, slot filling factor, electromagnetic load, and operation condition.

2.2. Stator MMF harmonics

Both armature windings arrangement and stator tooth-slot structures, independent of the rotor topology of PM machines, cause the stator MMF harmonics. The analytical method has been employed to analyze stator MMF harmonics. Assuming the armature current is replaced by the equivalent current sheet focusing on the notch, the space MMF can be expressed as

$$F(\theta)=\frac{F_v}{F_p}\cos(\Delta\theta) \tag{1}$$

where F_v is the amplitude of the vth order MMF harmonic and F_p is the amplitude of the working order harmonic. Moreover, the phase-A axis is selected as the reference position, namely $\Delta\theta$=0 (mech. deg.). Fig. 3 exhibits the stator MMF distributed along the circumference of the 9s8p, 18s8p, and 27s8p PM machines. It can be observed that the MMF of the 18s8p PM machine is axisymmetric, while those of 9s8p and 27s8p are not. This stator MMF distribution will cause an unbalanced radial magnetic force in the 9s8p and 27s8p PM machines. When the Fourier series is used to decompose the MMF and normalize each harmonic, which of the normalized MMF harmonic spectrum is depicted in Fig. 4. It can be found that the 9s8p PM machine has abundant MMF harmonics,

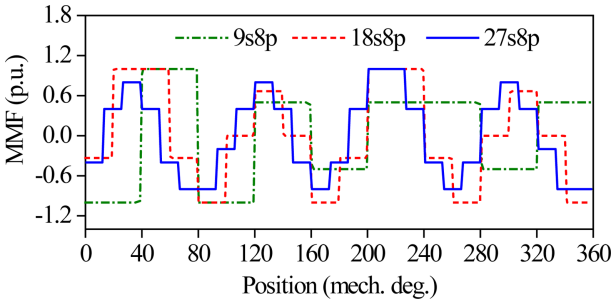

Fig. 3. (Color online) MMF distributed along the circumference of both machines.

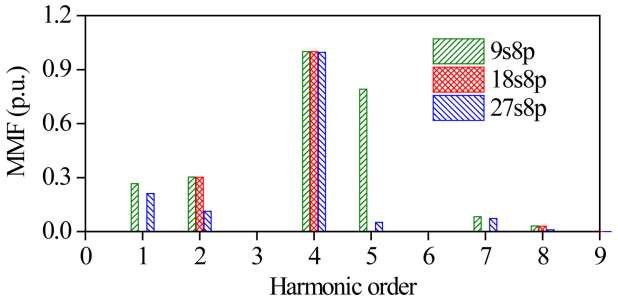

Fig. 4. (Color online) Normalized MMF harmonic spectrum of both PM machines.

such as 1st, 2nd, and 5th, while the 18s8p machine has less MMF harmonics which only has second-order sub-harmonic. The 27s8p machine has the first and second sub-harmonics, but their amplitudes are small.

From the perspective of MMF harmonics, 18s8p is the optimal choice for slot and pole coordination. However, the cogging torque ripple period of the 18s8p motor is small, so its cogging torque amplitude is relatively large. Therefore, considering the MMF harmonics and the cogging torque, the SPC of 27s8p is better than 18s8p.

In other word, the stator armature winding determines the stator MMF, so the MMF harmonics are related to the slot pole coordination and the stator topology.

2.3. Radial force harmonics

According to the Maxwell stress tensor method, the radial force per unit area of the air gap magnetic field produced by the PM machines can be expressed as

$$p_n(\theta,t)=\frac{B^2(\theta,t)}{2\mu_0} \tag{2}$$

where B is the flux density, and μ_0 is the vacuum permeability. As reported in [13], the lowest radial force harmonic (RFH) greatly influences PM machines, and the first-order RFH will cause unbalanced radial magnetic force. The lowest RFH is closely related to the greatest common divisor (GCD) of the slots and poles number, and Table 2 lists the lowest RFH of the different SPC PM machines. It can be seen that the lowest RFH of both the 9s8p and 27s8p PM machines is 1st, while that of 18s8p is second. Subsequently, The FEM calculates the RFH,

Table 2. Lowest RFH of the different SPC.

	FSCW	FSDW	
	Q=2p±1	GCD(Q,2p)=Even	kQ±h·2p=1
Slot/poles	9s8p	18s8p	27s8p
Lowest RFH	1	2	1

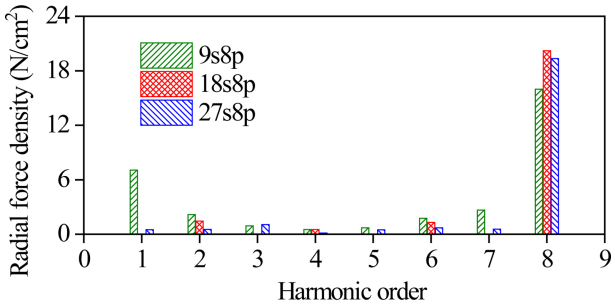

Fig. 5. (Color online) Comparison of RFH distribution of both PM machines.

and Fig. 5 compares their RFH spectrum in the same condition. It can be seen that the lowest RFH of both the 9s8p and 27s8p PM machines is 1st, while that of 18s8p is second. The first-order RFH of 9s8p is very high and probably causes high unbalanced radial magnetic force, which is not recommended. Since the first and second harmonics of the 27s8p machine are relatively small, its radial force is the smallest. The 18s8p machine has no unbalanced radial force, but the second radial force density harmonic will also cause a relatively small radial force. Regarding radial force harmonics, the 27s8p PM machine is the best section.

2.4. Cogging torque

The cogging torque originates from the interaction between the PMs and stator slots. Generally, the more time per turn of cogging torque is, the smaller the amplitude is. The relationship between the time per turn of cogging torque and GCD and the least common multiple (LCM) of stator slots and poles number as

$$\gamma = 2pQ / \mathrm{GCS}(Q,2p) = \mathrm{LCM}(Q,2p) \tag{3}$$

where γ is the time per turn of cogging torque. The LCM and GCD of slots and poles number of both machines are shown in Table 2. The magnitude of the cogging torque

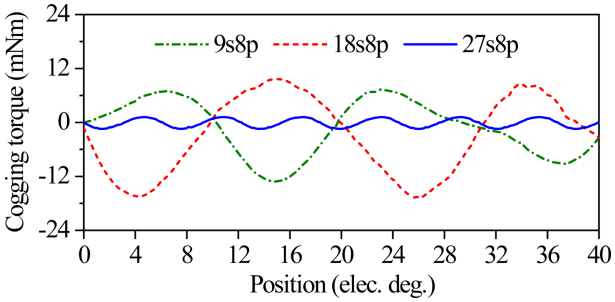

Fig. 6. (Color online) Cogging torque waveform of the three SPC PM machines.

Table 3. The LCM and GCD of the three SPC PM machine.

	9s8p	18s8p	27s8p
LCM (Q,2p)	72	72	216
Rate of LCM (Q,2p)	1	1	3
GCD (Q,2p)	1	2	1

can be pre-judged and compared through the machine SPC.

Fig. 6 presents the cogging torque of the three PM machines in a 1/9 mechanical period. It can be observed that the 9s8p and 18s8p machines have two electric periods, and the 27s8p one has six periods, which agrees with the result in Table 3. Besides, the amplitude of cogging torque of the 9s8p and 18s8p machines are nearly the same and more extensive than that of the 27s8p one. Comparing the analysis and simulation results, they are very consistent.

3. Selection of Rotor Topology

Four PM rotor topologies and their no-load magnetic lines, which include SPM, Spoke type, V-shape, and MR type, are described in Fig. 7. To ensure the mechanical strength of rotor PMs, a sleeve is adopted in SPM rotor topology. It can be found that the rotor topologies of SPM

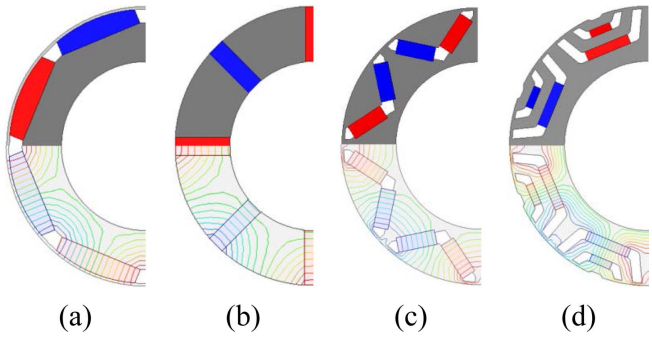

Fig. 7. (Color online) Rotor topologies. (a) SPM. (b) Spoke type. (c) V-shape. (d) MR type.

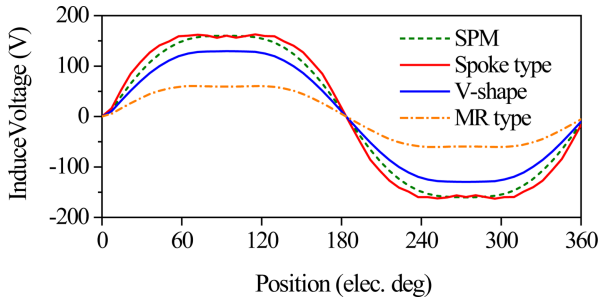

Fig. 8. (Color online) Back-EMFs of four PM machines.

and Spoke type are almost no flux leakage. Because of the magnetic bridge, the V-shape and MR-type rotor topologies have considerable magnetic leakage. The result is that the rotor topologies of SPM and Spoke type have large back-EMF than that of the V-shape and MR type.

3.1. No-load back-EMFs

The phase A no-load back EMF waveforms of four PM machines with different rotor structures are shown in Fig. 8. It can be seen that the no-load back EMF amplitudes of SPM and Spoke machines are more significant, and the no-load back EMF waveforms of SPM and V-shape machines have the highest sine degree. The back-EMF amplitude of the multilayer magnetic barrier structure machine is the smallest, and its waveform is similar to the Spoke-type machine, showing a flat top shape, which is beneficial to reduce the inverter capacity of the motor system. Besides, the multilayer magnetic barrier structure has a enormous reluctance torque than other structures, which is suitable for the weak magnetic operation of electric vehicles. Considering the machine's back-EMF and waveform sine degree, the V-shape rotor is an ideal choice [14].

3.2. Torque

In order to calculate the PM torque, the armature current is set to contain only the *q*-axis current component. The reluctance torque can be approximately obtained by setting the rotor PMs to vacuum when ignoring magnetic circuit saturation. Table 4 lists the calculation results of PM torque, reluctance torque, total torque, and torque ripple of the four-rotor topologies machine. It can be seen that the PM torque of SPM and spoke machines is relatively large, but their reluctance torque is minimal and can be almost ignored. In other words, the electromagnetic torque of these two types of motors is mainly permanent magnet torque. The reluctance torque of V-shape and MR-type motors is relatively large, especially for MR-type motors, whose reluctance torque accounts for about half of the total torque, which helps to improve the weak magnetic performance of the motor. In addition, the torque ripple of the SPM and V-shape structures is smaller than that of the spoke and MR-type motors. Therefore, the V-shape rotor structure is an ideal choice for the interior PM machine.

Table 4. Torque of four different rotor topologies.

	SPM	Spoke type	V-shape	MR type
Electrical load (A/cm)	100	100	100	100
PM usage (mm^3)	460	284	331.5	172
PM torque (Nm)	11.0	10	6.6	3.4
Reluctance torque (Nm)	0.1	1.2	3.2	3.5
Total torque (Nm)	11.3	11.5	10.1	7.2
Torque ripple (%)	1.7	5.9	1.6	6.9

3.3. Flux-weakening Performance

Below the rated speed, the control strategy of maximum torque per ampere (MTPA) is adopted, and above the rated speed, due to the limitation of DC bus voltage, the PM machine should work in the operation condition of flux-weakening to ensure that PM machines can operate at constant power at higher speed. The flux-weakening operation has two cases at the coordinate position of point A_3 as shown in Fig. 9. If the coordinate value of the A_3 point is within the current limit circle (that is, the $-E_0/X_d > i_s$), the maximum power output (MPO) track will fall outside the current limit circle. The flux-weakening field is only under ordinary flux-weakening control, depicted in Fig. 9(a). The theoretical maximum speed of the flux-weakening region can be derived as [15]

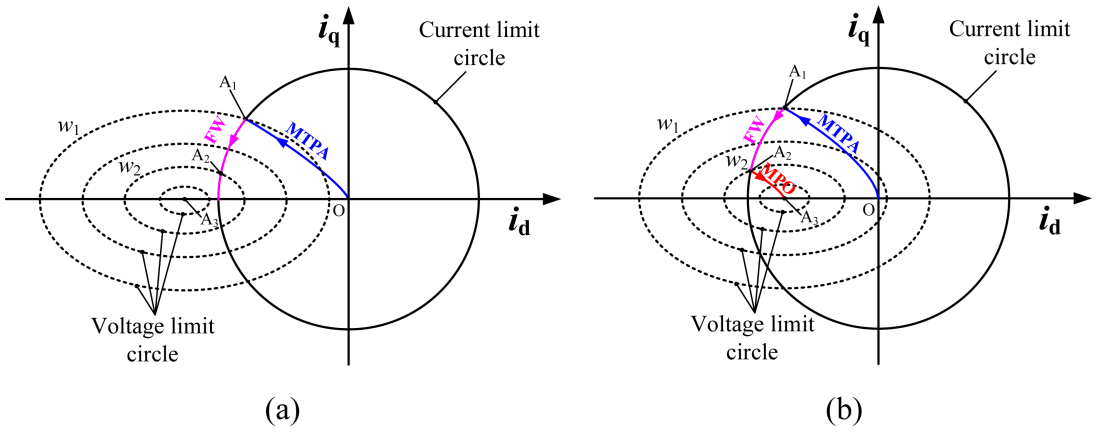

Fig. 9. (Color online) Schematic diagram of flux weakening control. (a) A_3 ($-E_0/X_d > i_s$). (b) A_3 ($-E_0/X_d < i_s$).

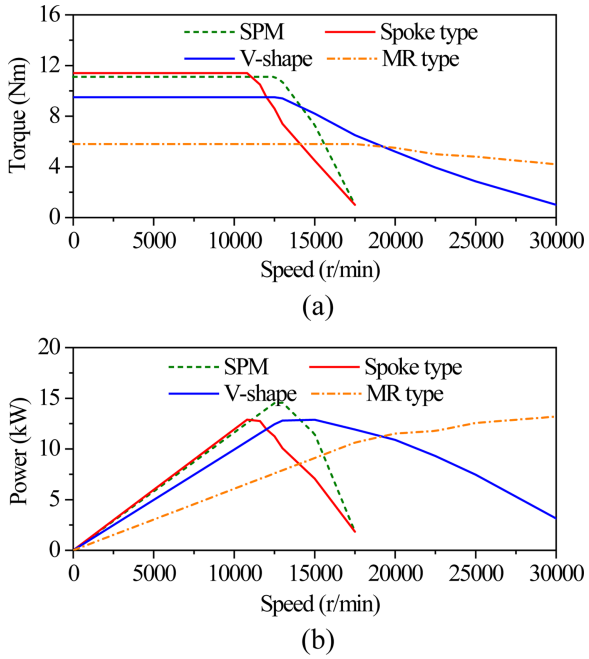

Fig. 10. (Color online) Torque- and power- speed curves. (a) Torque-speed. (b) Power-speed.

$$\omega_{\mathrm{r\,max}} = \frac{|u_{\mathrm{s}}|_{\max}}{E_0 + X_{\mathrm{d}} i_{\mathrm{d}}} \tag{4}$$

where w_{r} max is the theoretical maximum speed, $|u_{\mathrm{s}}|$ is DC bus voltage, and μ_0 is the vacuum permeability. Conversely, if the $-E_0/X_{\mathrm{d}} < i_{\mathrm{s}}$, the stator current control is divided into two parts in the flux-weakening region, including FW and MPO, as exhibited in Fig. 9(b). Obviously, in this case, the theoretical maximum speed is infinity.

The torque and power versus rotor speed performance at the same operation condition are plotted in Fig. 10. Obviously, it can be observed that the MR-type rotor topology has a more comprehensive constant power speed range and a relatively higher torque above the rated speed than the other designed PM machines, which is very suitable for electric vehicle applications. In addition, the V-shape machine has moderate flux-weakening performance and high torque at the rated speed. Comprehensively considering, the V-shape rotor topology is the optimal choice in this paper. Besides, it can be found that the rotor topology of SPM and Spoke type has a high torque in the constant torque region. However, the torque/power drop is pronounced above the base speed. In other words, both rotor topologies have poor flux-weakening performance, which is unsuitable for an occasion of high-speed range.

4. Design Optimization of 27s8p V-shape IPM Machine

4.1. Dimensional optimization

The dimensional optimization model of the stator slot and rotor topology is presented in Fig. 11, in which some of the primary dimension parameters are marked. The stator slot opening Bs0 and slot opening depth Hs0 are considered to fine-tune the *d*-axis inductance. Generally, the performance of a PM machine enhances as Tm is increased. However, it increases the cost of the PM machine. The air-gap length is assumed to be constant at 0.7 mm, considering the manufacturing tolerances and static and dynamic radial clearances. The B20AT1500_2DSF0.950 electrical steel is used for the stator and the rotor laminations, whereas the PM material NdFeB is considered with remanent flux density and relative recoil permeability of 1.28 T and 1.2, respectively. In order to meet the high-speed operation requirement for this PM machine, the magnetic bridges are designed between two adjacent opposite polarity PMs depicted in Fig. 11(b), which both keep the rotor stresses well below the yield strength of rotor material and provide PM support during operation. Fig. 12 shows the 2-D cross-section and 3-D impression drawing of the optimized V-shape IPM

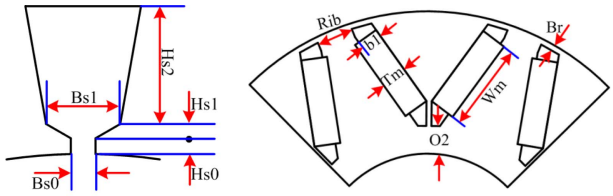

Fig. 11. (Color online) Dimensional optimization model. (a) Stator slot. (b) Rotor topology.

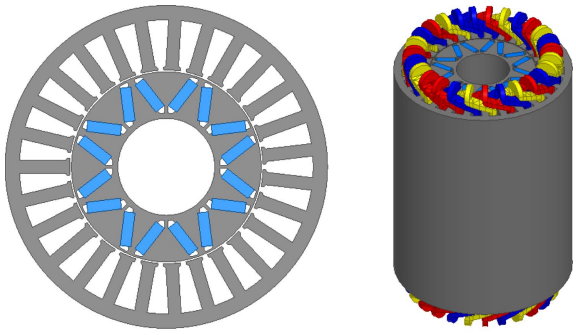

Fig. 12. (Color online) Optimized V-shape IPM machine. (a) 2-D section. (b) 3-D structure.

machine. It should be noted that the mechanical strength of the rotor structure is strengthened by connecting the adjacent permanent magnets through a magnetic bridge.

4.2. Rotor surface shaping

The 1/8 V-shape rotor topology models without and with rotor shaping are exhibited in Fig. 13. Two minimal parts are cut on the surface of the rotor yoke. Moreover, the magnetic path can be forced to change. The flux lines are shown in Fig. 14. Obviously, the magnetic path is changed in the position where the rotor yoke is shaped.

The A-phase no-load back-EMF with and without rotor shaping are plotted in Fig. 15. It is obvious that the no-load back-EMF of the machine with rotor shaping is better than that of one without rotor shaping because the magnetic path can be forced to change.

Fig. 13. Rotor surface shaping model. (a) Before. (b) After.

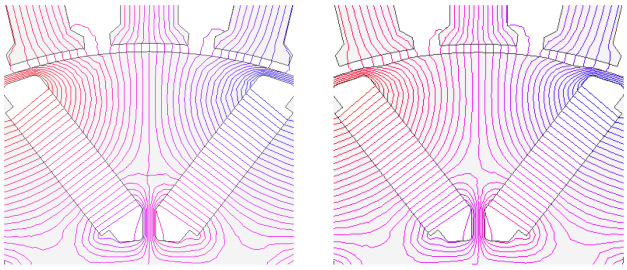

Fig. 14. (Color online) Flux magnetic lines before and after of rotor shaping. (a) Before. (b) After.

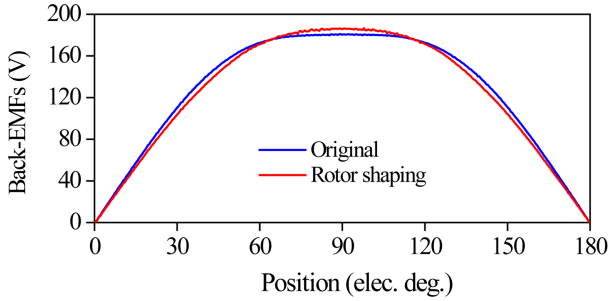

Fig. 15. (Color online) No-load Back-EMF with and without rotor shaping.

5. Rotor Mechanical Stress Analysis

The mechanical strength of IPM rotor topology is significant for high-speed machines, and the mechanical stress analysis is carried out using 2-D FEA at the 1.5 times higher maximum speed (about 16500r/min). Fig. 16 presents some analysis models of mechanical stress and the mesh of these rotor models, which include a V-shape without a magnetic bridge, a V-shape with a magnetic bridge, and a V-shape with a magnetic bridge and PMs. These models are a progressive relationship. It can be found that the meshes are small and uniform to ensure the accuracy of the FEM calculation. They have the same constraint, boundary, and operation conditions for a fair comparison. Besides, it is worth noting that to respond to the influence of the PM centrifugal force entirely, the volume of the PMs is slightly smaller than the PM slot, as shown in Fig. 16(c), so that the calculation results are not affected.

The software of ANSYS is employed to calculate the equivalent stress, and the analysis results are compared in Fig. 18. It should be noted that all results are magnified at the exact times of 1000 for precise observation. Besides, the outline of the black line indicates the undeformed rotor topology. In engineering, the tensile strength of steel and the tensile yield strength of the available silicon steel laminate is about 250 Mpa. It can be observed from Fig. 17 that the rotor model of a V-shape without a magnetic bridge suffers from immense stress and obvious deformation, and its maximum stress value is 89 Mpa within the safe range. With the existence of the magnetic bridge, the deformation has become very small, and the equivalent stress of the magnetic bridge at the end of the PM is significantly reduced, whose maximum stress value is 30 Mpa. Finally, when PMs are placed in the PM slot, compared with Fig. 17(b), the existence of the PMs has little influence on the equivalent stress and deformation of

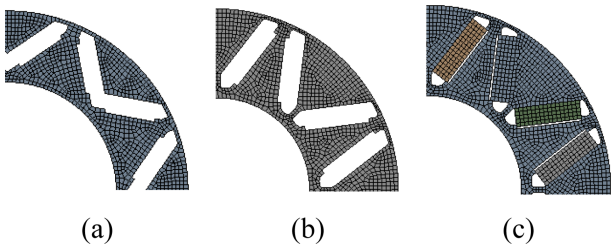

Fig. 16. (Color online) Mesh of different rotor topologies. (a) V-shape without magnetic bridge. (b) V-shape with magnetic bridge. (c) V-shape with magnetic bridge and PMs.

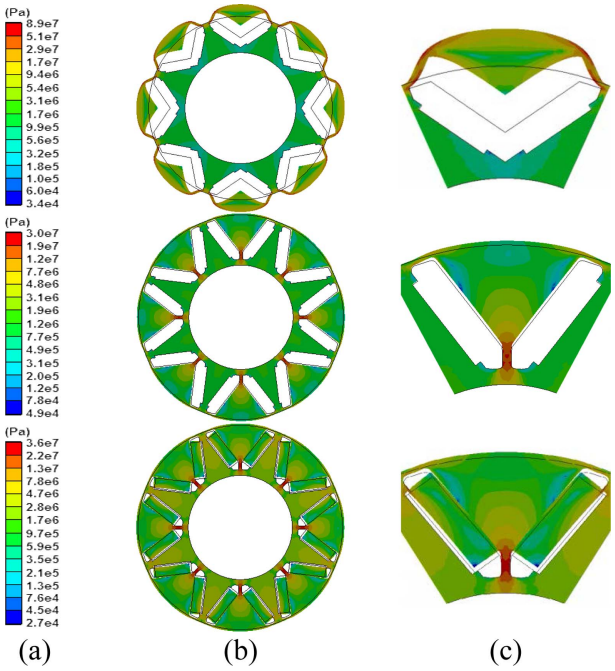

Fig. 17. (Color online) Stress and deformation. (a) Color scale. (b) Rotor. (c) Local amplification.

the rotor.

6. D-Q Axis Mathematical Model

The d-q axis mathematical model can analyze both analyze static and transient performance. In order to build a d-q axis mathematical model, the following assumptions are made

1) Ignoring the saturation of the machine core.

2) Ignoring eddy-current and hysteresis loss in the PM machine.

3) The stator armature current of the PM machine is a symmetrical three-phase sinusoidal current.

Transformation matrix:

$$C=\frac{2}{3}\begin{bmatrix}\cos(\theta) & \cos(\theta-120^\circ) & \cos(\theta+120^\circ)\\ -\sin(\theta) & -\sin(\theta-120^\circ) & -\sin(\theta+120^\circ)\\ 1/2 & 1/2 & 1/2\end{bmatrix} \quad (5)$$

Flux linkage equation

$$\begin{cases}\psi_d=\psi_f+L_d i_d\\ \psi_q=L_q i_q\end{cases} \quad (6)$$

Voltage equation

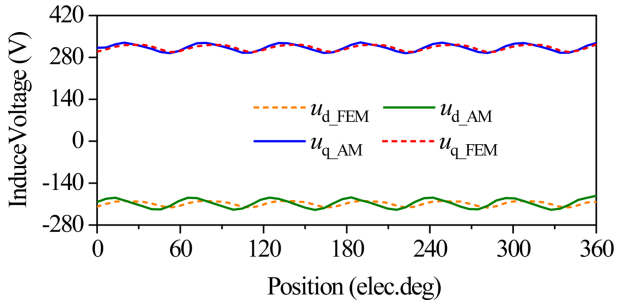

Fig. 18. (Color online) Voltage of d-q axis of both calculated method.

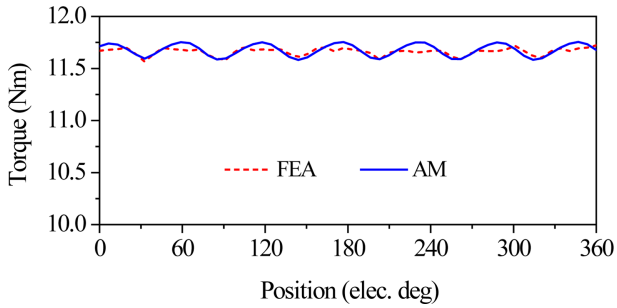

Fig. 19. (Color online) Electromagnetic torque of both calculated method.

$$\begin{cases}u_d=-\omega\psi_q+R_s i_d\\ u_q=\omega\psi_f+\omega\psi_d+R_s i_q\end{cases} \quad (7)$$

Torque equation

$$T_{em}=p\left(\psi_d i_d-\psi_q i_q\right) \quad (8)$$

where L_d and L_q are the *d-q* axis inductance, i_d and i_q are the *d-q* axis current, ψ_f is permanent-magnet flux linkage, R_s is phase resistance, and w is rotor angular velocity. Fig. 18 and Fig. 19 shows the analytical method (AM) results by the *d-q* axis mathematical model and compared calculation results with the finite-element method (FEM) results. From Fig. 18 and 19, it can be found that the calculation results of *d-q* axis mathematical model are in agreement with results of FEM simulation.

7. Experimental Validation

The 27s8p PM machine is prototyped to validate analytically calculated and FEM-predicted results. Fig. 20 exhibits the prototype photos of the V-shape IPM machine. The machine adopts fractional-slot winding, in which the coil pitch is 3. Besides, the rotor surface has been slightly modified to improve the back EMF waveform. The ventilation groove is designed on the stator

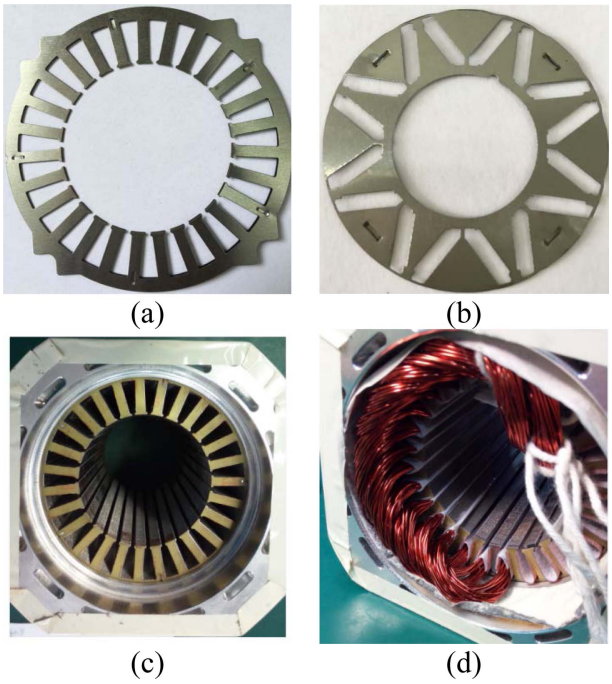

Fig. 20. (Color online) Prototype photoes. (a) Stator lamination for positioning. (b) Rotor lamination. (c) Stator. (d) Fractional-slot windings.

Fig. 21. (Color online) Measured phase no-load back-EMF of the PM machines.

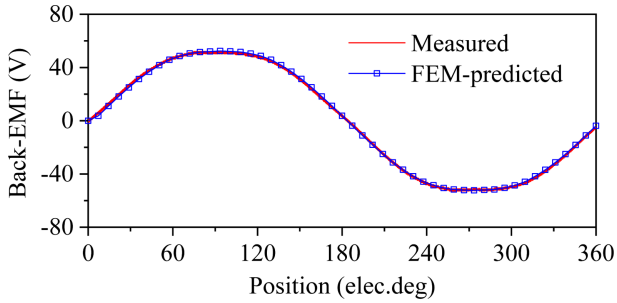

Fig. 22. (Color online) FEM-predicted and measured back-EMF of the 27s8p PM machine.

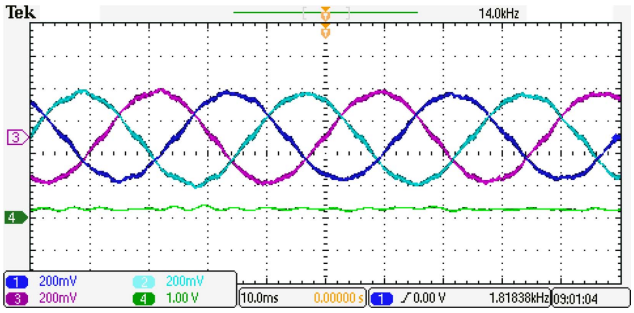

Fig. 23. (Color online) Measured phase current and torque.

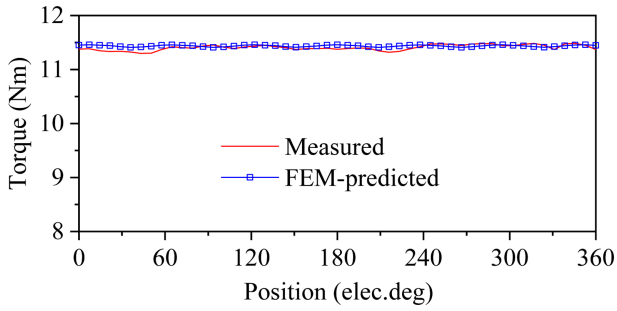

Fig. 24. (Color online) FEM-predicted and measured torque of the 27s8p PM machine.

surface to facilitate heat dissipation.

The measured back-EMF of the PM machines at the speed of 3500r/min is presented in Fig. 21. To compare the FEM prediction and measured results more clearly, Fig. 22 compares the FEM-predicted and measured back-EMF of the 27s8p PM machine. Due to the use of fractional-slot windings and the rotor modification, the back-EMF of the PM machine is very sinusoidal. Moreover, the measured back-EMF is in good agreement with the FEM-predicted one.

Fig. 23 shows the measured phase current, and the amplitude of the phase current is 18A. The amplitudes of the currents of the PM machine are not entirely equal. Since the sampling quality of the machine's platform is limited and the current returned from the sampling deviates from the actual current. The measured and FEM-predicted torque at the current of 18A is compared and presented in Fig. 24. The measured torque agrees with the FEM-predicted. The average torque value of the measured and the FEM-predicted are the same. However, the measured torque ripple is more significant than the FEM-predicted one. It is closely related to the quality of the above platform, and we will gradually improve the hardware platform in follow-up work.

8. Conclusion

This paper designs and analyzes an IPM machine

equipped with FSDW, which offers high torque density, high efficiency, and less torque ripple. Moreover, it reports the selection principle of SPC, and some electromagnet performances are compared. The research shows that the SPC dramatically influences the performance of the PM machine, and the 27s8p machine MMF harmonics, radial force density harmonics, and cogging torque are relatively small, which is an ideal SPC option. Besides, compared with other interior rotor structures, the V-shape rotor structure has better back EMF waveform, higher torque density, and a more comprehensive speed regulation range. Finally, The experimental test results agree with the finite element prediction results, which verifies the correctness of the finite element calculation.

Acknowledgement

The Natural Science Research Program of Jiangsu Colleges and Universities under Grant (23KJB470033).

References

[1] J. W. Jung, B. H. Lee, and D. G. Ahn, J. Magn. **27**, 379 (2022).
[2] W. Tong, S. Li, X. Pan, S. Wu, R. Tang, IEEE Trans. Energy Convers. **35**, 2191 (2020).
[3] T.-S. Kwon and S.-K. Sul, IEEE Trans. Ind. Appl. **42**, 1293 (2006).
[4] S. Duan, L. Zhou, and J. Wang, IEEE Trans. Ind. Appl. **24**, 1 (2014).
[5] P. B. Reddy, A. M. EL-Refaie, H. Kum-Kang, J. K. Tangudu, and T. M. Jahns, IEEE Trans. Energy Convers. **27**, 593 (2012).
[6] Y. Wang, R. Qu, and J. Li, IEEE Trans. Ind. Appl. **51**, 2208 (2015).
[7] J. Zheng, W. Zhao, J. Ji, and C. H. T. Lee, IEEE Trans. Ind. Electron. **69**, 1333 (2022).
[8] A. El-Refaie, IEEE Trans. Ind. Electron. **57**, 107 (2010).
[9] J. Zheng, J. Mao, and W. Zhang, IEEE Trans. Ind. Electron. **70**, 5410 (2023).
[10] S. Chung, J. Kim, Y. Chun, B. Woo, and D. Hong, IEEE Trans. Energy Convers. **30**, 103 (2015).
[11] J. Zheng, W. Zhao, J. Ji, J. Zhu, C. Gu, and S. Zhu, IEEE Trans. Ind. Electron. **65**, 8476 (2018).
[12] Z. Wu, W. Hua, C. Cheng, H. Zhang, and M. Hu, IEEE Trans. Ind. Electron. doi: 10.1109/TIE.2023.3260344.
[13] S. Zhu, J. Ji, and G. Liu, J. Magn. **24**, 657 (2019).
[14] C. Wang and Z. Q. Zhu, IEEE Trans. Ind. Appl. **56**, 1505 (2020).